Article

Electrochemically synthesized H_2O_2 at industrial-level current densities enabled by in situ fabricated few-layer boron nanosheets

Yuhan Wu[1,5], Yuying Zhao[2,3,5], Qixin Yuan[1], Hao Sun[2], Ao Wang[2], Kang Sun[2], Geoffrey I. N. Waterhouse [3], Ziyun Wang [3] ✉, Jingjie Wu [4] ✉, Jianchun Jiang [2] ✉ & Mengmeng Fan [1,2] ✉

Carbon nanomaterials show outstanding promise as electrocatalysts for hydrogen peroxide (H_2O_2) synthesis via the two-electron oxygen reduction reaction. However, carbon-based electrocatalysts that are capable of generating H_2O_2 at industrial-level current densities (>300 mA cm^{-2}) with high selectivity and long-term stability remain to be discovered. Herein, few-layer boron nanosheets are in-situ introduced into a porous carbon matrix, creating a metal-free electrocatalyst (B_n-C) with H_2O_2 production rates of industrial relevance in neutral or alkaline media. B_n-C maintained > 95% Faradaic efficiency during a 140-hour test at 300 mA cm^{-2} and 0.1 V vs. RHE, and delivered a mass activity of 25.1 mol $g_{catalyst}^{-1}$ h^{-1} in 1.0 M Na_2SO_4 using a flow cell. Theoretical simulations and experimental studies demonstrate that the superior catalytic performance originates from B atoms with adsorbed O atoms in the boron nanosheets. B_n-C outperforms all metal-based and metal-free carbon catalysts reported to date for H_2O_2 synthesis at industrial-level current densities.

Hydrogen peroxide (H_2O_2) is an indispensable oxidant in today's chemical industry, especially in the paper industry. Recently, the industrial-level H_2O_2 synthesis by the electrocatalyzing two-electron oxygen reduction reaction (2e$^-$ ORR) has emerged as a very promising alternative way to the traditional anthraquinone process in terms of energy efficiency, production costs and environmental friendliness[1,2]. Distributed electrochemical H_2O_2 synthesis can also resolve challenges around the storage and transportation of H_2O_2 at high-concentrations.

Although carbon-based catalysts have demonstrated decent 2e$^-$ ORR performance under laboratory conditions, these carbon catalysts generally show poor durability under industrial-level current densities. In the past few years, enormous effort has been devoted to designing

and modulating the composition and nanostructure of carbon catalysts to improve the 2e$^-$ ORR selectivity and durability, using strategies such as heteroatom doping[3], defect engineering[4] or nanostructure engineering[1,5,6]. Among these approaches, heteroatom (e.g., O, N, S, P, B, etc.) doping accompanied by the introduction of abundant carbon defects (e.g., pentagonal and heptagonal) into carbon materials is the simplest and most promising route for achieving the optimal catalytic performance[1,7,8]. Currently, carbon materials functionalized with oxygen functional groups (e.g., -COOH, C=O and C-O-C) or oxygen doped are considered the promising metal-free catalysts for H_2O_2 synthesis (selectivity over 90% in alkaline electrolyte)[9,10]. Nevertheless, these oxygen functionalized carbon catalysts suffer from high resistance and unstable catalytic activity under modest current densities (e.g., only

[1]Jiangsu Co-Innovation Center of Efficient Processing and Utilization of Forest Resources, Nanjing Forestry University, Nanjing 210037, China. [2]Key Lab of Biomass Energy and Material, Jiangsu Province; Jiangsu Co-Innovation Center of Efficient Processing and Utilization of Forest Resources, Institute of Chemical Industry of Forest Products, Chinese Academy of Forestry, Nanjing 210042, China. [3]School of Chemical Sciences, The University of Auckland, Auckland 1010, New Zealand. [4]Department of Chemical and Environmental Engineering, University of Cincinnati, Cincinnati, OH 45221, USA. [5]These authors contributed equally: Yuhan Wu, Yuying Zhao. ✉e-mail: ziyun.wang@auckland.ac.nz; jingjie.wu@uc.edu; jiangjc@caf.ac.cn; fanmengmeng370@njfu.edu.cn

11-hour stability at 50 mA cm^{-2})[9]. Density functional theory (DFT) simulations show that among different dopants (e.g., C, N, O, S, P), B atoms doped into carbon matrices have nearly-zero overpotentials for the formation of H$_2$O$_2$, suggesting outstanding catalytic performance[11]. However, the B-doped carbon electrocatalysts reported to date do not show excellent 2e$^-$ ORR performance, for example, only delivering ~90% H$_2$O$_2$ selectivity in a 0.1 M KOH electrolyte at 0.4–0.7 V vs. RHE and 80% H$_2$O$_2$ selectivity in 0.1 M Na$_2$SO$_4$ at 0.1–0.35 V vs. RHE[11]. The sub-optimal catalytic performance of B-doped carbons can be attributed to low B atom content or inappropriate B configurations (e.g., BC$_2$O, BCO$_2$)[12]. Moreover, as reported for the other heteroatoms, the B dopants in carbon matrices are gradually lost under long-term testing at high current densities via hydrogenation and reconstruction of carbon heterocyclic structures[11,13]. As such, there are very few reports relating to stable B-doped carbon catalysts for ORR. As a result, the relationship between B structure and catalytic performance under industrial-level current density (>300 mA cm^{-2}) remains elusive. Few-layer boron nanosheets with a stable crystal structure (B$_n$), represent a very promising 2D boron-based material in electrochemistry due to its unique structure and electronic properties (e.g., high carrier mobility, superconductivity). As such, few-layer boron nanosheets offer an exciting platform for the electronic structure tuning and design of stable B-based carbon catalysts for H$_2$O$_2$ synthesis and other applications[14,15].

In this work, we report a one-step "bottom-up" strategy to in situ fabricate few-layer boron nanosheets (B$_n$) on porous carbon matrix (B$_n$-C) using small-molecule precursors (citric acid, boric acid) and copper (II) acetylacetonate. Through a straightforward pyrolysis treatment of a dried hydrogel containing the precursors and copper acetylacetonate, boron nanosheets are uniformly dispersed on the porous carbon matrix. Spectroscopic analysis reveals the presence of a limited number of oxygen-containing functional groups on the surface of the boron nanosheets. DFT calculations demonstrate that these surface oxygen groups on the boron nanosheets modulate *OOH adsorption strength during the 2e$^-$ ORR, thereby inhibiting *OOH reduction to H$_2$O and enhancing the selectivity and rate of H$_2$O$_2$ production. Compared to single B atom doping, the integration of boron nanosheets increases the density of active sites, enhances the catalytic activity of B atoms, and facilitates O$_2$ adsorption, resulting in significantly improved catalytic performance for 2e$^-$ ORR in both alkaline and neutral electrolytes at industrially relevant current densities. In a neutral electrolyte, the B$_n$-C delivered over 90% H$_2$O$_2$ selectivity after 12-hour durability tests in rotating ring disk electrode (RRDE) tests and a Faradaic efficiency >90% over a 140-hour durability test at a current density of 300 mA cm^{-2} in a flow cell. Further, a mass activity up to 25.1 molg$_{catalyst}^{-1}$ h^{-1} was achieved in a flow cell. The overall 2e$^-$ ORR performance of B$_n$-C surpasses that of all previously reported metal and metal-free carbon-based electrocatalysts. Finally, we designed an in situ H$_2$O$_2$ consuming system for lignin depolymerization, employing papermaking waste black liquor powder as a lignin source. The successful recycling of aromatic carbon compounds from lignin is demonstrated.

Results

Synthesis, morphology and structure of catalysts

Previous studies have shown that the Cu (100) surface can induce the formation of micrometer-scale single crystalline borophene[16]. Herein, we fabricated boron nanosheets on a porous carbon matrix (B$_n$-C) through annealing a hydrogel containing boric acid, citric acid and copper (II) acetylacetonate (Fig. 1a). The presence of Cu in the hydrogels promoted the formation of boron crystal islands with a specific growth orientation[16]. The obtained B$_n$-C was washed with hydrochloric acid and hot water, dried, and then subjected to detailed structural characterizations and electrochemical measurements.

An annealing temperature of 900 °C was determined to be optimal based on the nanostructure and catalytic performance (Supplementary Figs. 1–3). Further, control samples were fabricated under similar experimental conditions, but without copper (II) acetylacetonate, boric acid, or copper (II) acetylacetonate and boric acid. The corresponding samples are denoted herein as B single atom doped carbon (B$_1$-C), Cu catalyzed carbon (pure C), and blank porous carbon (blank C), respectively. In the XRD pattern, the B$_n$-C sample (Fig. 1b) showed peaks at 16.4°, 17.8° and 26.4°, corresponding to the (110), (104) and (211) planes, respectively, of β-rhombohedral boron crystalline structure (PDF#80-0322)[14,15,17]. The B$_n$-C showed the enhanced peak intensities at (110) and (211), indicating boron nanosheets of few layers thickness, which is attributable to the confinement effect of the carbon substrate. Compared to the Pure C and Blank C, the B$_n$-C and B$_1$-C catalysts showed more intense Raman bands at 446 cm^{-1} to 606 cm^{-1} associated with E_g mode of B-B clusters[14,15,18,19], and as expected for few-layer boron nanosheets bonding with O atoms (Fig. 1c). When using boric acid or copper (II) acetylacetonate into the precursor mixture, the as-prepared carbon samples showed an intense (002) peak in carbon matrix, with the B$_n$-C sample having intense (002) peak ~24.5 ° (at higher angle than the other samples), which can be attributed to the catalytic carbon crystal growth involving layered H$_3$BO$_3$ and Cu catalysts[20]. The introduction of B atoms or boron nanosheets added many defects into the carbon matrix, hence the B$_n$-C and B$_1$-C exhibited slightly higher I$_D$/I$_G$ ratios in the Raman spectra compared to the other catalysts (Supplementary Fig. 4)[21]. As metal Cu catalyzes the graphitization of carbon materials, the B$_n$-C showed a lower I$_D$/I$_G$ value than that of B$_1$-C[22]. N$_2$ adsorption/desorption measurements at 77 K (Fig. 1d) showed B$_n$-C to possess a high specific surface area (SSA) of 811.8 m^{2}g^{-1} and contain abundant mesopores (2–7 nm) (Fig. 1d inset), which were expected to offer an abundance of active sites and accelerate mass transfer, respectively[21], during the ORR. Compared to B$_1$-C, the higher surface area and porosity in B$_n$-C can be attributed to the addition of Cu (II) acetylacetonate which was converted into Cu oxide nanoparticles (a hard-template) during the annealing progress[23,24]. In the HR-TEM image (Fig. 1e), the B$_n$-C had porous structure with abundant boron crystal nanosheets with the lateral sizes ranging from a few nanometers to a few hundred nanometers (Supplementary Fig. 5). The atomic force microscopy (AFM) images for B$_n$-C showed the thickness of boron nanosheets to be ~10 nm, indicating a few layers for the boron nanosheets (Supplementary Fig. 6). At higher magnification (Fig. 1f), lattice fringes with spacings of 0.56 nm and 0.44 nm could be observed, corresponding to the (110) and (104) planes, respectively, of β-rhombohedral boron[15,25]. The FFT pattern of a (110) facet (Fig. 1f inset) further confirmed the crystalline nature of the few-layer boron nanosheets[15,25]. As reported previously for the growth of borophene or graphene on Cu films by chemical vapor deposition[16,26], the realization of few-layer boron nanosheets in the B$_n$-C can be attributed to the catalytic behavior of Cu. The B$_1$-C catalyst prepared without adding copper (II) acetylacetonate showed fewer boron crystal domains, with these being of small lateral size (only a few nanometers) in Supplementary Fig. 7. The blank C catalyst prepared without adding H$_3$BO$_3$ or copper (II) acetylacetonate exhibited fewer graphene domains compared to the Pure C catalyst (prepared with adding copper (II) acetylacetonate) as shown by the data in Supplementary Figs. 8, 9. Elemental mapping of B$_n$-C showed a uniform distribution of boron nanosheets and single B atoms on the carbon matrix, respectively (Fig. 1g and Supplementary Fig. 10). In the FT-IR spectrum of B$_n$-C (Supplementary Fig. 11), a characteristic B-H-B mode was seen at 1591 cm^{-1}, along with a B-O stretching mode (1252 cm^{-1}) and C-B stretching mode (1161 cm^{-1}), indicating the existence of few-layer boron nanosheets[27], O atoms bonded to B atoms on the surface of boron nanosheets[19], and the immobilization of boron nanosheets on the carbon matrix[14], respectively.
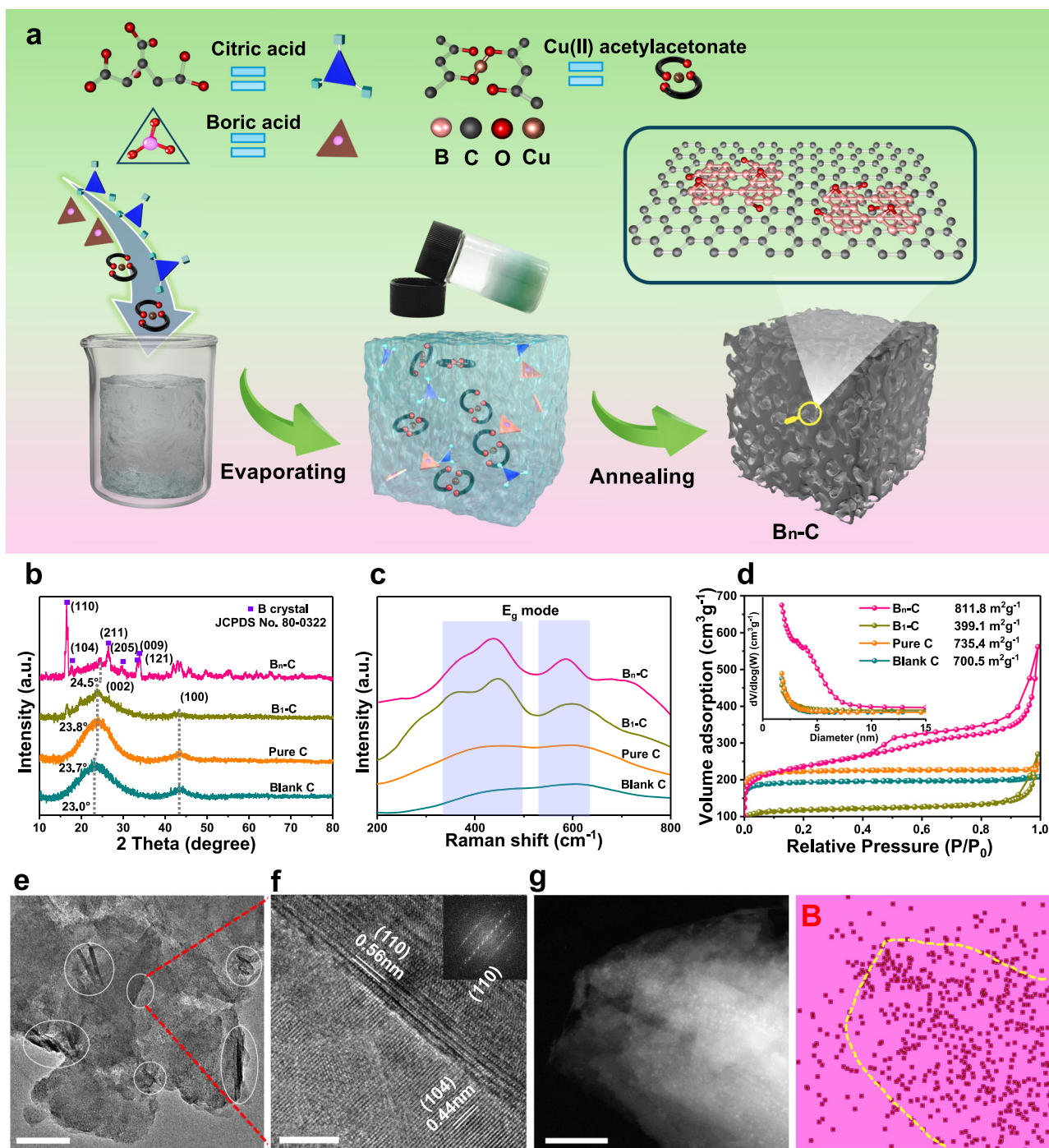
Fig. 1 | Synthesis and characterizations of B_n-C. a Schematic illustration of the fabrication of B_n-C. **b** The XRD patterns. **c** Raman spectra. **d** N_2 adsorption–desorption isotherms (inset, the pore diameter distributions) for B_n-C and control catalysts. **e** Low-magnification HR-TEM image of B_n-C, scale bar 100 nm. **f** High-magnification HR-TEM image and the FFT pattern (inset) of B_n-C, scale bar 5 nm. **g** High-angle annular dark-field scanning transmission electron microscopy (HAADF-STEM) image and boron EDS mapping image (red dots) for B_n-C, scale bar 100 nm.

Composition and electronic properties of catalysts

The electronic structure of B_n-C was further investigated by X-ray photoelectron spectroscopy (XPS) and X-ray absorption near-edge structure (XANES). As shown in the high-resolution C 1 s XPS spectrum of B_n-C (Fig. 2a), the existence of a B-C peak at 284.0 eV indicated a covalent interaction between the boron nanosheets and the carbon matrix. The inductively coupled plasma mass spectrometry (ICP-MS) showed the B content in B_n-C to be 0.19 wt.% lower than that of B_1-C (0.42 wt.%) in Supplementary Table 1. The high-resolution B 1 s XPS spectrum of B_n-C (Fig. 2b) was deconvoluted into peaks due to B-B (187.0 eV and

188.4 eV), B-C (190.5 eV), and B-O (192.3 eV), offering additional evidence for the presence of boron nanosheets and B single atoms[14,16]. Two B-B peaks at 187.0 eV and 188.4 eV are assigned to the B-B bonds in the boron nanosheets, and the B-B-C bonds formed between the boron nanosheets and carbon matrix, respectively[14–16,28,29]. Compared to the B_1-C (Supplementary Fig. 12), the B_n-C catalyst showed more intense B-B signals, consistent with the B_n-C catalyst containing much more boron nanosheets (in agreement with the XRD results). The high-resolution O 1 s XPS spectrum for B_n-C exhibited an intense peak at 531.8 eV (48.7% of all O species for B_n-C, versus 38.6% for the Pure C catalyst) in Fig. 2c,
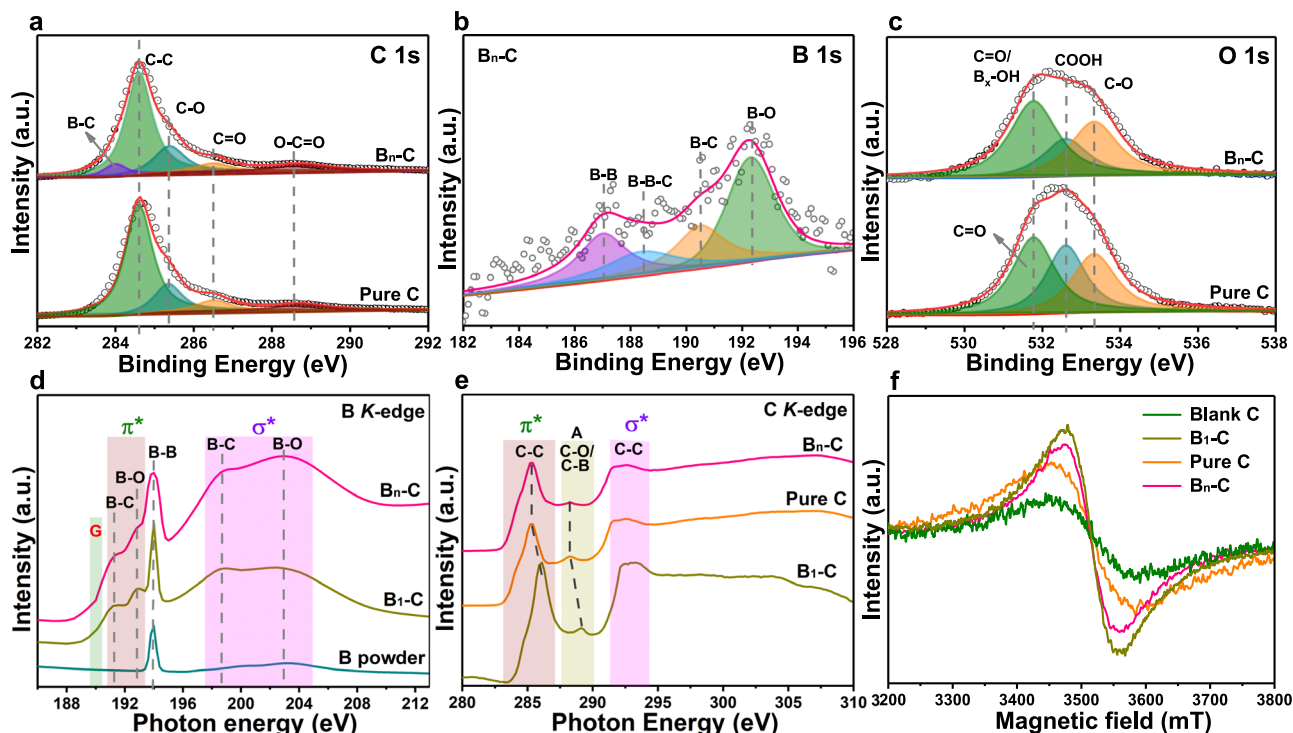
Fig. 2 | Electronic structure and environment of Bn-C. a–c High-resolution C 1 s, B 1 s and O 1 s XPS spectra. **d** B K-edge XANES spectra for B_n-C, B_1-C, B powder. **e** C K-edge XANES spectra for B_n-C, B_1-C and Pure C. **f** EPR signals of B_n-C and control catalysts.

which can be attributed to the O atoms on the surface of few-layer boron nanosheets in the form of bridging oxygen (i.e., B-O-B)[30,31]. This is consistent with previous reports, which showed that borophene reacted with O atoms to enhance its own stability under an O_2 atmosphere[18,32]. In order to further probe the local environment of the few-layer boron nanosheets in carbon matrix, B K-edge XANES spectra were collected. The B K-edge XANES spectra for B_n-C, B_1-C and boron powder (Fig. 2d) all showed a peak at 193.9 eV, assigned to the transition of B 1 s electrons into an unoccupied B $2p_z$ orbital and associated with B-B bonds in few-layer boron nanosheets[33]. The B_n-C sample had an obvious G peak at 189.4 eV, which can be the attributed to the fewer layer and larger size of boron nanosheets than that of the boron powder and B_1-C, respectively[34]. The B_n-C and B_1-C catalysts each exhibited two peaks in the π^* and σ^* regions. In the π^* region, the two peaks are associated with B atoms coordinated with C and O atoms in a sp^2 hybridization, while the broader peaks in the σ^* region can be assigned to B−C and B−O bonding (i.e., sp^3 hybridization)[35,36]. In the C K-edge XANES spectra (Fig. 2e), the peaks at ~285.0 eV result from the excitation of an electron from the C 1 s level into unoccupied π^* orbitals (typical for sp^2-bonded carbon atoms such as C=C and C=O), whilst the broad peak at ~292.0 eV results from an electronic transition from the C 1 s level into an empty σ^* state (σ^* band) associated with sp^3-hybridized carbons (i.e., C-C bonds or C-O)[34,36]. The broad features at 288.2 eV are assigned to the C- B/C-O and C-O bonds in the A regions of B_n-C and Pure C, respectively[35,37]. Compared to the other catalysts, the C K-edge spectrum of B_1-C (prepared without adding copper II acetylacetonate) was shifted to higher photon energies, indicating the lower degree of graphitization in the carbon matrix[34]. The data again confirms that the presence Cu during the synthesis of the catalysts enhanced the graphitization of carbon matrix. Next, electron paramagnetic resonance (EPR) spectroscopy data was collected to explore the interfacial states between few-layer boron nanosheets and the carbon matrix in the B_n-C and B_1-C catalysts. Compared to the other catalysts, the B_n-C and B_1-C catalysts had a stronger EPR signal at ~2.003 G factor (Fig. 2f), which is assigned to the lattice defects and unpaired electrons on the boron nanosheets or their

interfaces with the carbon matrix in Fig. 2f[38]. The slightly higher signal density in B_1-C is attributed to more carbon defects as demonstrated by the higher I_D/I_G ratio in the Raman spectra (Supplementary Fig. 4)[39].

2e⁻ oxygen reduction performance via RRDE measurements

The 2e⁻ ORR electrocatalytic performance of B_n-C and other catalysts were evaluated in O_2-saturated 0.1 M KOH (Fig. 3a−c) and 0.1 M Na_2SO_4 (Fig. 3d−f) solutions using a RRDE with a calibrated collection efficiency of 0.37 determined using the [Fe (CN_6)]⁴⁻/[Fe (CN_6)]³⁻ redox probe (Supplementary Fig. 13). We first excluded the interference of residual Cu on the catalytic performance by ICP-MS measurements and poisoning experiments using KSCN, with no obvious poisoning effect observed (Supplementary Fig. 14). The catalyst loading was also optimized (Supplementary Fig. 15). In the LSV polarization curves, the B_n-C had a much higher disk current (from O_2 reduction) and ring current (from H_2O_2 oxidation at a constant potential of 1.20 V vs. RHE) compared to the other catalysts, indicating superior 2e⁻ ORR catalytic activity. The B_n-C and B_1-C catalysts had a 2e⁻ ORR onset potential of 0.81 V vs. RHE (determined at ring current density of 0.3 mA cm⁻² after calibration of the collection efficiency). The onset potentials were superior to most previously reported 2e⁻ ORR catalysts, indicating that the introduction of few-layer boron nanosheets enhanced the ORR kinetics (Supplementary Table 2). The H_2O_2 selectivity and electron transfer number (n) (Supplementary Fig. 16) were calculated from the LSV curves (Supplementary Fig. 17). For the B_n-C catalyst, the H_2O_2 selectivity remained over 95%, and the n value lower than 2.1, over a wide potentials window of 0.4 V−0.7 V vs. RHE, highlighting a highly selective 2e⁻ ORR pathway. The Pure C catalyst with a high specific surface area (735.4 m²g⁻¹) also exhibited a high H_2O_2 selectivity (> 90%) which can be attributed to the abundant graphene sheets with edge defects and many oxygen-containing functional groups[40,41]. The durability of B_n-C was measured through the chronoamperometry method with continuous 12-hour operation at 0.65 V vs. RHE. The disk and ring currents showed almost no change and the H_2O_2 selectivity remained above 92% over the duration of the test in Fig. 3c,
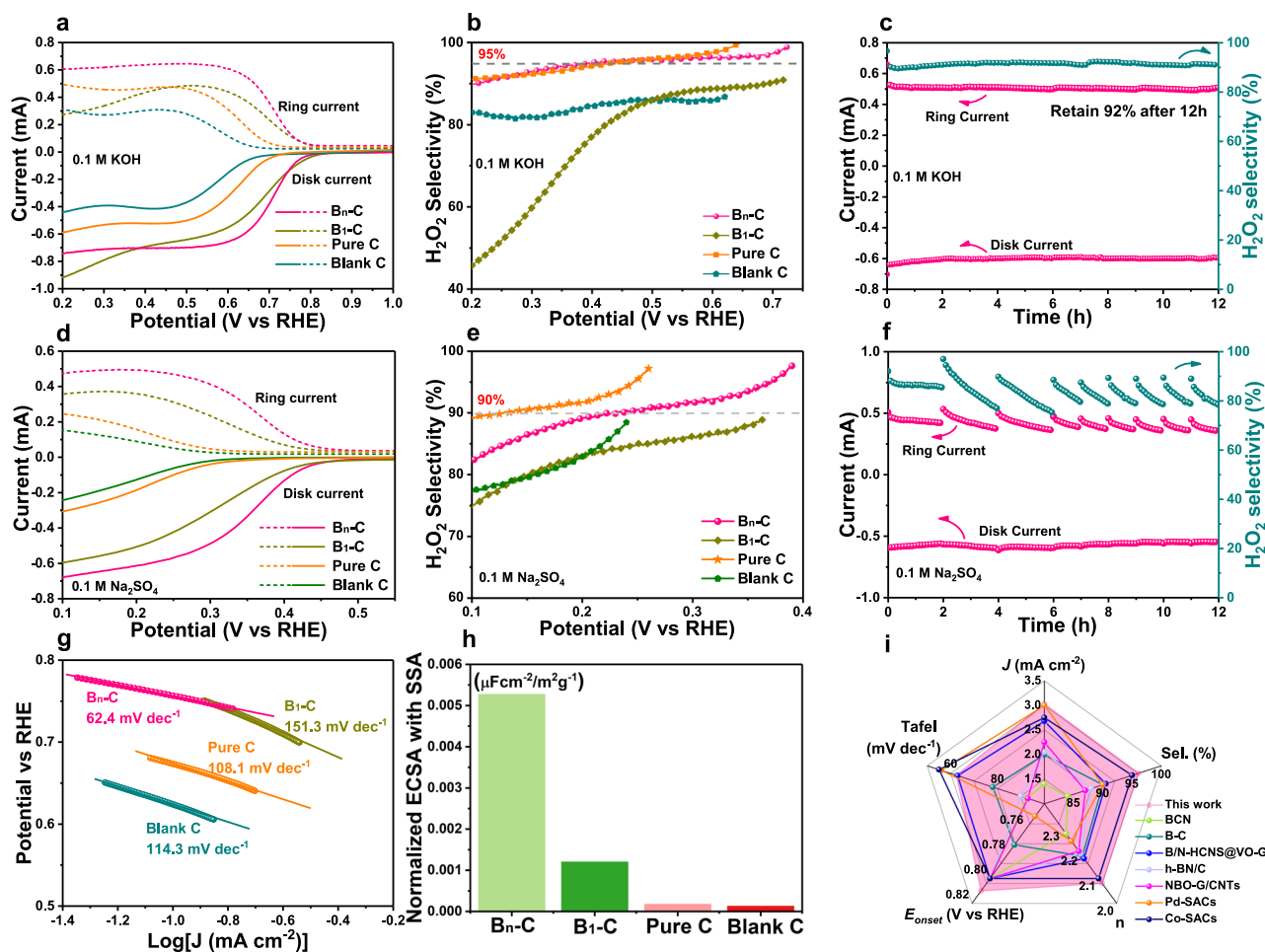
Fig. 3 | Electrocatalytic performance of catalysts: H_2O_2 production in O_2-saturated alkaline and neutral electrolytes. a–c Electrocatalytic measurements in an O_2-saturated alkaline electrolyte (0.1 M KOH, pH = 13), ORR polarization curves (solid lines) with the corresponding H_2O_2 current on ring electrode (dashed lines) at 1.2 V vs. RHE at 1600 rpm without iR-compensation (the ring current had a collection efficiency of 0.37), the LSV curves were measured three times in Supplementary Fig. 17 (**a**), H_2O_2 selectivity (**b**), chronoamperometry stability test for 12 hours at 0.65 V vs. RHE (**c**). **d–e** Electrocatalytic measurements in an O_2-saturated neutral electrolyte (0.1 M Na_2SO_4, pH = 7), ORR polarization curves (**d**), the LSV curves were measured three times in Supplementary Fig. 19. H_2O_2 selectivity (**e**), chronoamperometry stability test for 12 hours at 0.25 V vs. RHE (the line beak of ring current was due to the repeatedly electrochemical reduction of Pt ring) (**f**). **g** Tafel slopes in 0.1 M KOH. **h** ECSAs normalized against BET SSAs. **i** Radar plot comparing the $2e^-$ ORR performance of B_n-C with many previously reported catalysts (Supplementary Table 2).

demonstrating a remarkable stability for $2e^-$ ORR. After the durability test at high current density, the used B_n-C catalyst exhibited the same porous morphology to the fresh B_n-C catalyst, suggesting good robustness (Supplementary Fig. 18). Similar to the alkaline electrolyte studies, the B_n-C also showed good $2e^-$ ORR catalytic performance in a neutral electrolyte (0.1 M Na_2SO_4), including a high disk and ring current (Fig. 3d), high H_2O_2 selectivity of over 90% (Fig. 3e and Supplementary Fig. 19) and remarkable durability (Fig. 3f) as summarized in Supplementary Table 3. In a 12-hour durability test, the disk current also showed almost no change in the neutral electrolyte. Due to H_2O_2 oxidizing the Pt ring in a neutral electrolyte, the Pt ring was cleaned every 2 hours. The Tafel slope of B_n-C derived from the LSV curve in Fig. 3a was calculated to be 62.4 mV dec^{-1}, superior to the B_1-C (151.3 mV dec^{-1}), pure C (108.1 mV dec^{-1}) and blank C (114.3 mV dec^{-1}), implying very fast kinetics for $2e^-$ ORR (Fig. 3g, and Supplementary Fig. 20). The electrochemically active surface areas (ECSA) of the catalysts were evaluated by the double-layer capacitance (C_{dl}) method, thus providing information about the availability of active sites in the various catalysts (Supplementary Fig. 21). The ECSA values were normalized by BET specific surface area (SSA) using the formula of ECSA/SSA. The B_n-C had the highest normalized ECSA value, 4.4 times higher

than that of B_1-C in Fig. 3h, and vastly superior to the Pure C and Blank C, strongly suggesting that the B_n-C catalyst possessed an abundance of electrochemical active sites. The disk current density of B_n-C did not scale with the normalized ECSA value due to the well-known mass transfer restrictions in RRDE measurements[42]. We further compared the catalytic performance of B_n-C with other reported carbon-based catalysts and highly efficient single metal atom catalysts (SACs) for $2e^-$ ORR focusing on five key performance indicators: current density (J), H_2O_2 selectivity ($Sel.\%$), electron transfer number (n), Tafel slope and onset potential (E_{onset}). The radar chart (Fig. 3i) showed that the B_n-C delivers the more promising overall performance among the catalysts.

We also explored the catalytic performance of B_n-C catalysts prepared using transition metal precursors other than copper (II) acetylacetonate, such as iron (III) acetylacetonate, cobalt (II) acetylacetonate, nickel (II) acetylacetonate. The corresponding B_n-C samples were denoted herein as B_n-C-1, B_n-C-2, and B_n-C-3, respectively. The synthesis conditions for B_n-C-x (x = 1, 2, 3) catalysts were identical, except for the metal precursor used. The XRD patterns for the B_n-C-x catalysts (Supplementary Fig. 20) all showed peaks for borophene, indicating that like copper, these transition metals all promoted the formation of borophene-carbon composites from boric acid and citric

acid. However, compared to the B_n-C-1 and B_n-C-3, the B_n-C-2 sample contained much larger borophene sheets (similar to those obtained for B_n-C) as revealed in the HR-TEM images (Supplementary Fig. 23–25). As expected, the B_n-C-2 delivered much better 2e⁻ ORR performance than the B_n-C-1 and B_n-C-3 catalysts, with the performance of B_n-C-2 close to B_n-C prepared using Cu (II) acetylacetonate (Supplementary Fig. 26), The data further demonstrates that large-size borophene sheets were beneficial for improving the 2e⁻ ORR performance.

Next, we sought to increase or decrease the O content in the B_n-C and explored the effect of O content on ECSA and ORR catalytic performance (Supplementary Fig. 27). The B_n-C was weakly oxidized with H_2O_2 (to form the O-B_n-C) or reduced by H_2/Ar atmosphere (to form the R-B_n-C). The O content increased from 10.9 at.% for B_n-C to 13.2 at.% for the O-B_n-C and decreased to 7.6 at.% for the R-B_n-C. As the O content increases, the ECSA of B_n-C gradually increases. The O-B_n-C showed a more positive onset potential than B_n-C, while the R-B_n-C gave a lower disk current, ring current and lower H_2O_2 selectivity. Therefore, increasing O content was beneficial to enhance the catalytic performance of 2e⁻ ORR, with the B_n-C having a near-optimal O content.

H_2O_2 production at a high rate in a flow cell

Based on the RRDE screening tests and electrochemical analyses, the B_n-C catalyst was identified as a near ideal electrocatalyst for 2e⁻ ORR. To validate its promise for industrial application at high current densities, a standard three-electrode flow cell setup (Supplementary Fig. 28) was assembled to evaluate its 2e⁻ ORR performance in 1.0 M KOH and 1.0 M Na_2SO_4 electrolytes. The B_n-C loaded gas diffusion layer (GDL) electrode (concentration of 0.2 mg cm⁻²), Ni foil and Ag/AgCl electrode were used as the working electrode, counter electrode and reference electrode, respectively. The H_2O_2 concentration (C_{H2O2}) was determined by a titration method using $Ce(SO_4)_2$, and the FE was further calculated based on the C_{H2O2} produced and amount of charge consumed with reaction time. The FE is different from the "selectivity", the former was calculated based on the percentage of produced H_2O_2 and consumed electrons in bulk electrolysis in either H-type cell or flow cell, while the H_2O_2 "selectivity" is the molar proportion of H_2O_2 calculated via RRDE measurements[6]. In the alkaline and neutral electrolytes, the LSV curves all showed greatly increasing current density, over 95% FE and a linearly increasing H_2O_2 production rate as the potential was swept negatively (Fig. 4a, b and Supplementary Fig. 29). A chronoamperometry method was used to test catalyst durability. The potential was fixed in 0.42 V vs. RHE with 80% iR-compensation to achieve a current density of 300 mA cm⁻² in 1.0 M KOH. During the 140-hour test, the current density was maintained without noticeable degradation, with the FE to H_2O_2 remaining over 90% (Fig. 4c). A total H_2O_2 production of 21.4 g was achieved after 140-hour and the corresponding mass activity was 29.3 molg$_{catalyst}$⁻¹ h⁻¹. Similarly, in 1.0 M Na_2SO_4, the potential was fixed in 0.10 V vs. RHE and the current density set at 300 mA cm⁻². In the 140-hour test, the change of current density was negligible with the FE remaining higher than 95%, the total H_2O_2 production of 19.4 g with a mass activity of 25.1 molg$_{catalyst}$⁻¹ h⁻¹ (Fig. 4d). Compared to the reported state-of-the-art stability of metal or metal-free catalysts measured at high current density (>50 mA cm⁻²), our B_n-C catalyst offered good 2e⁻ ORR stability at high current densities, coupled with superior FE and yield rate (Fig. 4e and Supplementary Table 4). Overall, the B_n-C catalyst retained a high activity (high current density) and a high FE without noticeable degradation during long-term stability testing, confirming it as a promising candidate for industrial H_2O_2 electrosynthesis.

Depolymerization of lignin in black liquid from papermaking

The paper industry produces a massive amount of alkaline black liquid waste (rich in lignin). This black liquid causes pollution and represents a waste of natural resources[43]. Lignin, as one of main components of plant-based biomass feedstocks, is a promising though largely untapped source of aromatic chemicals[44]. Generally, the lignin in black liquid is removed in a combustion process[44], which is both environmentally unfriendly and inefficient. Depolymerizing lignin with H_2O_2 in an alkaline environment is therefore an attractive alternative, since it could yield valuable aromatic compounds for the chemical industry. In particular, lignin-derived monolignols monomers, such as p-hydroxyphenyl (H), sinapyl (S) and guaiacyl (G), can be used as raw material for producing many daily-use chemicals. Herein, we aimed to develop an electrochemical system for delignifying black liquid (Fig. 5a). The black liquid used in this research was obtained from Huatai paper plant in Shandong province of China (Fig. 5a inset). In the LSV curves in 0.5 M KOH (Fig. 5b and Supplementary Fig. 30), the setup showed a high current density up to 450 mA cm⁻² at 0.45 V vs. RHE without interference from the black liquid (150 mg L⁻¹), demonstrating the catalytic stability of B_n-C catalyst. After the treating black liquid (concentration of 990 mg L⁻¹) using in situ produced H_2O_2 over 22 hours at -300 mA cm⁻² and 0.5 V vs. RHE, the black liquid became colorless (Fig. 5c, inset). In the UV-vis spectra, the typical adsorption peaks of lignin at -340 nm were replaced by the peaks for aromatic oligomers or monomers in Fig. 5c. The liquid chromatography-mass spectroscopy (LC-MS) spectrum further demonstrated the efficient depolymerization of lignin (Supplementary Fig. 31)[45,46]. Throughout the 22-hour testing period, the black liquid was continuously added into the system, while both the current density and FE (maintained over 90%) exhibited minimal variation, underscoring the remarkable catalytic activity and stability of B_n-C for H_2O_2 production for simultaneous lignin depolymerization (Fig. 5d).

Mechanistic investigation to explain electrocatalytic performance of B_n-C

To explore the active sites and reaction mechanism over the B_n-C catalyst, in situ Raman spectroscopy was applied to study the ORR in 0.1 M KOH electrolyte using the setup shown in Fig. 6a and Supplementary Fig. 31. As the applied potential was decreased from 0.8 to 0 V vs. RHE, two bands located at 1150 cm⁻¹ and 1520 cm⁻¹ gradually intensified, with these bands able to be readily assigned to the adsorbed OOH* and O_2* formed during 2e⁻ ORR, respectively (Fig. 6b)[13]. The Raman spectrum at 0 V vs. RHE was further deconvoluted into four bands which were assigned to carbon defects (D_1), graphitic carbon (G), amorphous carbon bonding with heteroatom or oxygen species (D_3), and disordered graphite with A_{1g} symmetry (D_4)[47,48]. The D_4 and D_3 bands appeared to intensify when a negative potential was applied, owing to overlap with the signals of adsorbed O_2* and OOH* species, indicating the defective C atoms, doped B atoms also made contribution to the good 2e⁻ ORR performance of B_n-C (Fig. 6c)[4,11,49]. Next, O_2-temperature-programmed desorption (O_2-TPD) was applied to investigate the O_2 adsorption capacity of the catalyst (Fig. 6d), an essential prerequisite for ORR. The B_1-C and B_n-C showed O_2 desorption peaks at 88 °C and 262 °C which could readily be assigned to physisorbed and chemisorbed oxygen species, respectively. Due to lack of suitable active sites, the Pure C showed no obvious O_2 adsorption. Compared to the O_2 physisorption in B_1-C, the B_n-C catalyst showed the enhanced O_2 chemisorption indicating that boron nanosheets promote the entrapment of O_2 from gas bubbles[50].

DFT calculations were subsequently carried out to probe the catalytic activity origin of few-layer boron nanosheets in B_n-C. As demonstrated by our structural characterization studies and previous research[30,31], the structure of B_n-C was simplified with one single-layer borophene (B_n) bonding with single-layer graphene by B-C bonds at the edge and O atoms are adsorbed on the surface of B_n (Supplementary Fig. 32). The pure borophene without O adsorption shows a too high free energy to be protonated for the *OOH intermediate (Supplementary Fig. 33). There are three possible O adsorption modes on the surface of borophene (top O, bridge O and hollow O), with the
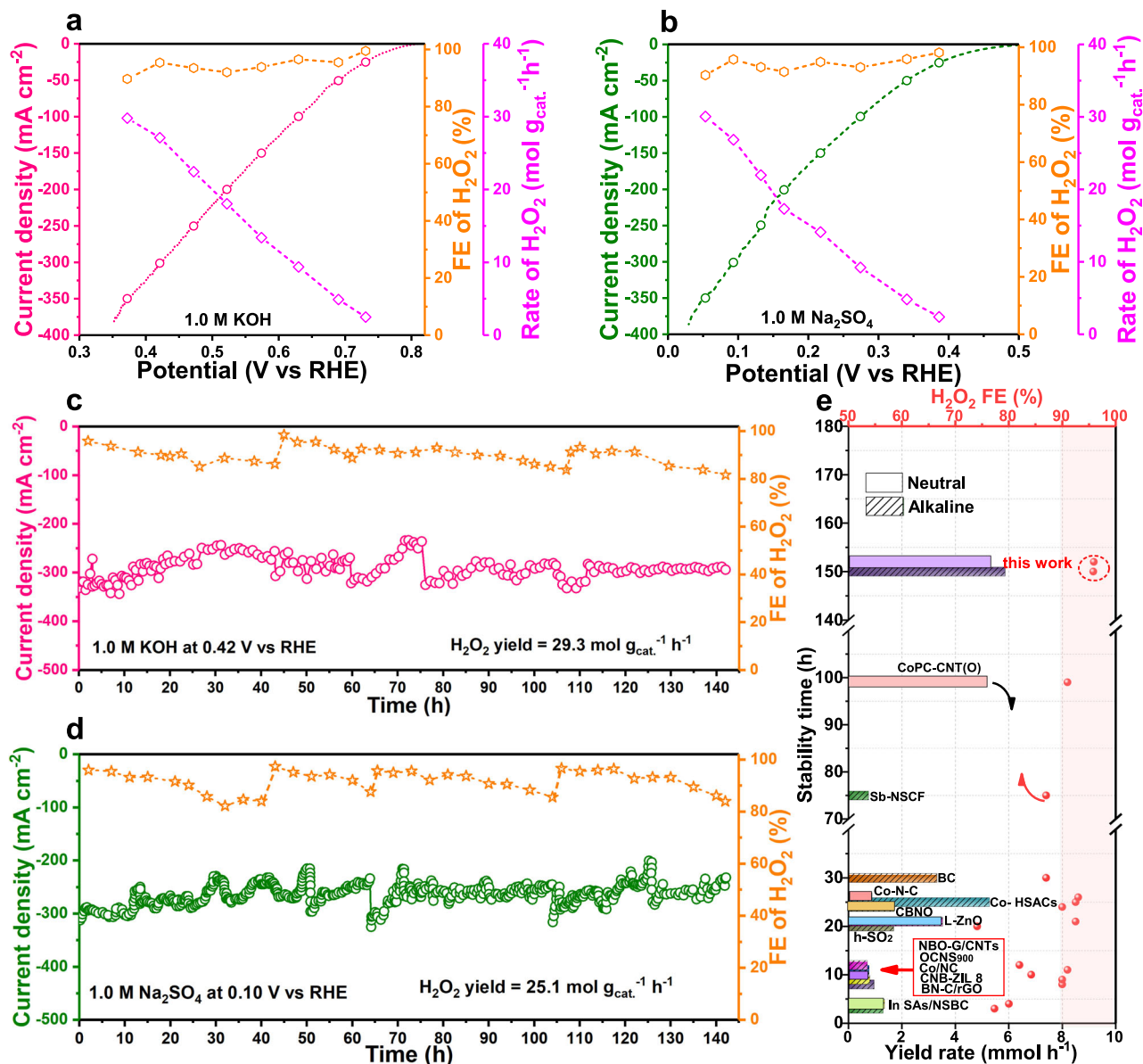
Fig. 4 | H2O2 production tests at high current densities in a flow cell. a, b LSV curves for 2e⁻ ORR in 1.0 M KOH and 1.0 M Na_2SO_4 electrolytes with 80% iR-Compensation (0.84 ± 0.09 Ω for 1.0 M KOH and 3.13 ± 0.13 Ω for 1.0 M Na_2SO_4). Corresponding FEs and production rates of H_2O_2 under different current densities are shown. The LSV curves were measured three times in Supplementary Fig. 29. **c, d** 140-hour stability test for B_n-C at 300 mA cm⁻² in 1.0 M KOH at 0.42 V vs. RHE and in 1.0 M Na_2SO_4 at 0.10 V vs. RHE, respectively. **e** Performance comparison of catalysts in a flow cell in terms of durability, FE and yield rate (Supplementary Table 4).

former being more effective in modulating the ORR intermediates (Supplementary Fig. 34). The B_n-C models with different numbers of top and bridge O atoms (O_x-B_n-C, where x = 1−9 represents the number of O atoms), along with B_1-C and Pure C models, were designed (Fig. 6e and Supplementary Fig. 35, 36). The O atoms bonded on the surface of B_n can modulate the adsorption capacity of neighboring B atoms in the plane of B_n towards ORR intermediates (*OOH, *OH, and *O). The free-energy diagram for O_2 reduction via both the 2e⁻ pathway and the 4e⁻ pathway are shown in Fig. 6f and Supplementary Fig. 37, 38. Comparing different O atoms coverages, the $O_8\_B_n$-C model was the better one. The Gibbs free adsorption energy (ΔG_{OOH*}) for *OOH intermediate species on the catalyst surface is often used as a descriptor to correlate with theoretical predictions of the 2e⁻ ORR. When the ΔG_{OOH*} of structures are closest to the most suitable value (4.22 eV), the ideal $U_{limited}$ (0.70 eV) for producing H_2O_2 will be achieved. The $O_8\_B_n$-C was closest to the top of the overpotential volcano in Fig. 6g and

Supplementary Table 4, exhibiting an overpotential of only 0.69 eV, indicating the good 2e⁻ ORR activity. Under the condition of electrode potential U = 0.7 V and U = 1.23 V, the step from O* to OH* was greatly inhibited on the $O_8\_B_n$-C sites, demonstrating that 2e⁻ pathway was more likely to occur than 4e⁻ pathway (Fig. 6h).

At the equilibrium potential for H_2O_2 production (U = 0.7 V vs. RHE), the rate-determining step (RDS) at $O_8\_B_n$-C site is the first electron transfer from O_2 to *OOH. This requires an energy of only 0.01 eV, which was much lower than the RDS energy (1.946 eV) for *OOH protonation on blank B_n-C without O atoms (Supplementary Fig. 39). The DFT results demonstrated that the blank B_n-C was inert for ORR and the O coverage can promote the generation of more B atoms active sites in the plane of B_n. To investigate the impact of O coverage on the surface of B_n for the production of the *OOH intermediate, we examined the electron density difference in $O_8\_B_n$-C with adsorbed *OOH intermediates (Supplementary Fig. 40) demonstrating that the surface
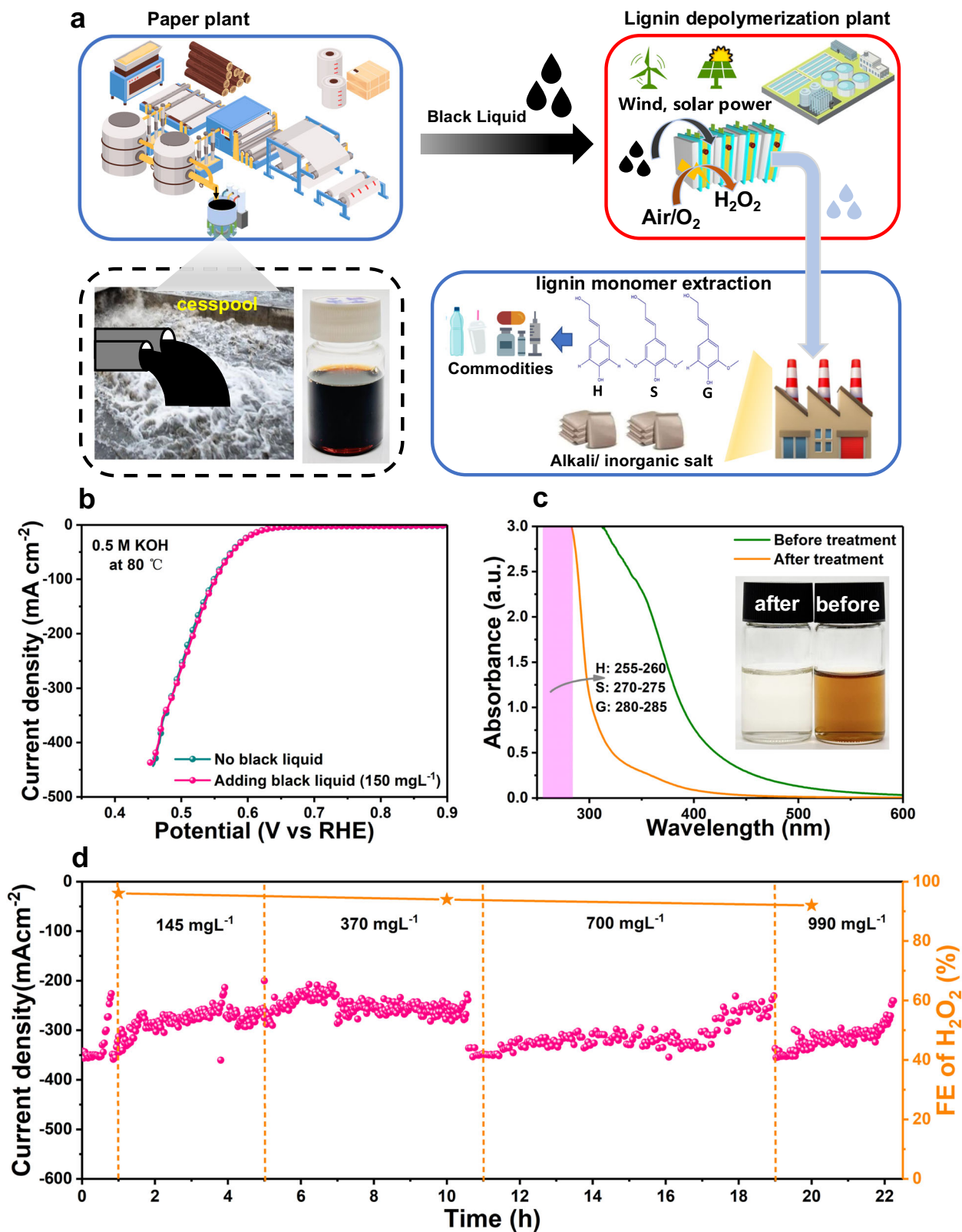
Fig. 5 | Depolymerization of lignin in black liquid from papermaking.
a Schematic illustration showing depolymerization of lignin in papermaking black liquid using in situ electrochemically synthesized H_2O_2 (inset, the black liquid cesspool, and solution). **b** The LSV curves with and without black liquid (150 mg L^{-1}) addition in 0.5 M KOH electrolyte with 80% iR-compensation (resistance value is 2.62 ± 0.15 Ω) measured three times (Supplementary Fig. 30). **c** UV-vis spectra before and after treating black liquid (inset: the photograph of black liquid solution before and after treatment). **d** Stability test with continuous addition of black liquid.
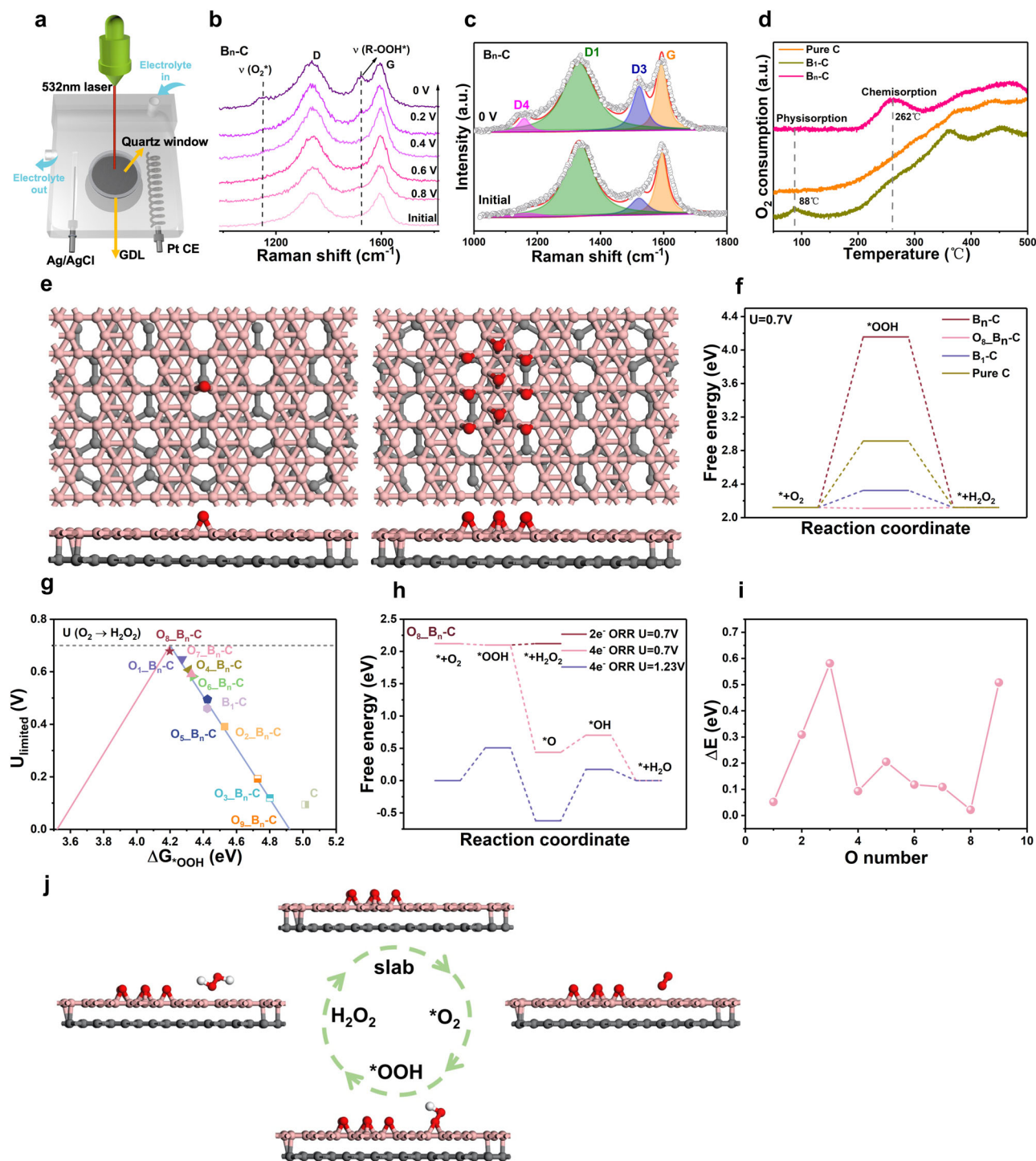
Fig. 6 | Catalytic mechanism for H_2O_2 production process. a Setup for in situ Raman measurements. **b** In situ Raman spectra of B_n-C during ORR at the potentials from 0.8 to 0 V vs. RHE. **c** Fitted Raman spectra of B_n-C with and without a potential of 0 V vs. RHE. **d** The O_2-TPD profiles for B_n-C, B_1-C and Pure C. **e** Models of boron nanosheets dispersed on graphene (B_n-C) with one to nine O atoms (gray, pink and red representing C, B and O atoms, respectively). **f** Free energy diagram of 2e[-] ORR (gray, pink and red representing C, B and O atoms, respectively). **g** ORR simulated activity volcano plot of samples. **h** Free energy diagram of 2e[-]/4e[-] ORR on the O_8-B_n-C. **i** Reaction barrier changes of *OOH intermediate for different number of O atoms. **j** Catalytic mechanism of O_2 reduction to H_2O_2 on $O_8\_B_n$ -C.

O atoms facilitated the migration of electrons from proximal B atoms to the adsorbed *O_2, thus activating the neighboring B atoms as catalytic sites, thereby enhancing the formation and production rate of the *OOH intermediate. The effect of different number of O atoms on the formation of *OOH was further explored (Fig. 6i), and we constructed curves of the energy barrier as a function of the number of O atoms. The energy barrier fluctuated upon increasing the number of O atoms.

Although the various $O_x\_B_n$-C models differ in their catalytic activity for 2e[-] ORR, most of the models had catalytic activity and selectivity superior to the single B atom model. As seen from the O_2-TPD tests, O_2 is readily chemisorbed on B_n under an O_2 atmosphere[31], ensuring a high activity of B atoms on the plane of B_n for 2e[-] ORR. The B atoms nearby the B_x-O structure on the B_n plane showed a weakened capability to forming B-O bonds due to the inductive effect of B_x-O groups,

which prevents the complete coverage on the surface of B_n by O atoms. These B atoms as active sites, have the appropriate binding energy for an O_2 molecule by forming an intermediate of B-(*OOH)-B. Therefore, the partial O atom coverage on B_n not only kept the charge transfer intact but also tuned the electronic structure to boost reactant adsorption and catalytic activity[51]. The $2e^-$ ORR mechanism (O_2 to H_2O_2) and the electroreduction process are shown in Fig. 6j. O_2 molecule adsorbs on the catalyst, forming *O_2, which receives an electron and proton to become a *OOH intermediate. This intermediate further accepts an electron and a proton to produce H_2O_2 that then desorbs from the catalyst. The catalytic cycle then continues since the surface is then free to adsorb new O_2 molecule.

Discussion

We successfully synthesized a B_n-C electrocatalyst consisting of few-layer boron nanosheets in a porous carbon matrix. The large size of the boron nanosheets was due to the presence of copper (II) acetylacetonate in the hydrogel precursor (which also contained boric acid and citric acid). The B_n-C was shown to be a highly efficient and durable electrocatalyst for $2e^-$ ORR. In flow cell tests under industrial-level current densities ($300\,mA\,cm^{-2}$), the B_n-C catalyst delivered unprecedented H_2O_2 synthesis performance in both alkaline and neutral media (FE over 90% in $1.0\,M$ KOH and $1.0\,M\,Na_2SO_4$ at $300\,mA\,cm^{-2}$). Structural characterization studies and DFT simulations showed that the O atoms on the surface of the boron nanosheets effectively activate adjacent B atoms on the B_n plane for efficient $2e^-$ ORR, by tuning the adsorption energy of the *OOH intermediate. Meanwhile, the borophene promoted O_2 adsorption, with the resulting enrichment effect improving mass transfer during ORR. As a practical demonstration, the B_n-C was successfully applied as the cathode in a H_2O_2 electrolyser system for in situ lignin depolymerization (i.e., converting black liquid from papermaking into simple aromatic compounds). This work opens up vistas for the design of carbon-based catalysts for H_2O_2 production at industrial current densities.

Methods

Chemicals and materials

Citric acid ($C_6H_8O_7$, 99.5%), boric acid (H_3BO_3, 99.5%), copper (II) acetylacetonate ($Cu(C_5H_7O_2)_2$, 97%), iron (III) acetylacetonate ($Fe(C_5H_7O_2)_3$, 98%), cobalt (II) acetylacetonate ($Co(C_5H_7O_2)_2$, 97%), nickel (II) acetylacetonate ($Ni(C_5H_7O_2)_2$, 95%), potassium hydroxide (KOH, 95%), sodium sulfate (Na_2SO_4, 99%), and cerium sulfate ($Ce(SO_4)_2$, 97%) were purchased from Macklin Co., Ltd. (Shanghai, China). Ethanol (C_2H_6O, 99.5%) and isopropanol (C_3H_8O, 99.5%) were purchased from Macklin Co., Ltd. (Shanghai, China). Commercial Boron powder (<5 μm, ≥94%) was purchased from Aladdin Co., Ltd. (Shanghai, China). Nafion solution (5 wt.%) and Nafion 117 proton exchange membrane were purchased from Du Pont Co., Ltd. The gas diffusion carbon (HCP120) was purchased from HESEN Co., Ltd. (Shanghai, China).

Synthesis of catalysts of B_n-C, B_1-C, Pure C and Blank C

To prepare the B_n-C catalyst, 5.0 g of citric acid, 5.0 g of H_3BO_3 and 0.2 g copper (II) acetylacetonate ($Cu(acac)_2$) were first dissolved into 80 mL of DI water, and then the resulting solution stirred at 80 °C for 10 hours to evaporate the water. The powder mixture was then further dried at 80 °C for 10 hours in an oven. The powder mixture was then annealed at 900 °C for 2 hours under an Ar atmosphere (200 sccm). After natural cooling to room temperature, the B_n-C product was washed three times with $1.0\,M$ hydrochloric acid and hot deionized water (100 °C), then dried at 50 °C in a vacuum oven. B_1-C was prepared by the same way as B_n-C, except that no $Cu(acac)_2$ was used in the synthesis. Pure C was prepared by the same way as B_n-C, except that no H_3BO_3 was used in the synthesis. Blank C was prepared by the same way as B_n-C, except that neither $Cu(acac)_2$ or H_3BO_3 were used in the synthesis.

Synthesis of catalysts of B_n-C-x (x = 1, 2, 3)

The preparation conditions of the B_n-C-x catalysts were the same as B_n-C, expect that ($Cu(acac)_2$) was replaced an equimolar amount of iron (III) acetylacetonate, cobalt (II) acetylacetonate or nickel (II) acetylacetonate, respectively.

Synthesis of B_n-C-x (x = 700, 800, 900, 1000)

Except for the annealing temperature, the other preparing conditions of B_n-C-x are same to those of B_n-C.

Synthesis of O-B_n-C and R-B_n-C

In total, 20 mg of B_n-C catalyst was added to a mixed solution consisting of 20 mL of deionized water and 20 mL of H_2O_2 (30 wt.%), after which the black suspension was heated and stirred in a water bath at 60 °C for 12 hours. After washing and drying the O-B_n-C catalyst was obtained. The O-B_n-C catalysts were obtained by annealing the B_n-C catalysts in a 5% H_2/Ar mixed atmosphere (20 sccm) under annealing conditions of 5 °C min^{-1} ramping up to 300 °C and holding for 2 hours.

ICP-MS measurement

Electrolyte samples were from the fresh alkaline electrolyte ($1.0\,M$ KOH) and the used electrolyte after electrochemical reaction were studied by ICP-MS. For the catalyst samples, 5 mg of catalyst was added into a beaker containing 5 mL of concentrated HNO_3 and 5 mL of concentrated $HClO_4$. The mixture was heated to a boil and then 1 mL of concentrated HNO_3/$HClO_4$ was slowly added until the catalyst had completely dissolved. Finally, the solution was diluted to 100 mL in a volumetric flask by adding DI water. The solution was used for ICP-MS test. A blank solution was prepared by the same method (without any catalyst).

Characterization

HR-TEM images were obtained on a Talos F200s transmission electron microscope (FEI), equipped with a Super-X EDS Detector (FEI) for EDS elemental mappings. AFM data was completed by atomic force microscope (BRUKER Dimension Icon). XPS data were obtained on a K-Al_α X-ray electron spectrometer (XPS) System (Thermo Scientific). ICP-MS data was obtained on an Inductively coupled plasma mass spectrometer (Agilent 5110OES). XRD data were obtained on a D8 FOCUS X-ray diffractometer (Bruker, using a Cu K$_\alpha$ radiation, λ = 0.154 nm). Raman spectra were collected on an inVia Raman spectrometer (Renishaw), equipped with a 532 nm laser. Fourier Transform Infrared spectra were acquired on a IS10 FTIR spectrometer (Nicolet). The surface area and pore distribution of samples was determined from N_2 adsorption-desorption isotherms collected at 77 K on a ASAP2460 gas adsorption analyzer (Micromeritics). XANES spectra were collected at the national synchrotron radiation laboratory (NSRL) in total electron yield (TEY) mode. The base pressure in the UHV chamber throughout the measurements was ~2×10^{-10} mbar. LC-MS data was measured by liquid chromatography-mass spectroscopy (Shimadzu LC-MS2050).

Electrochemical measurements on RRDE

Electrochemical measurements were performed using a standard three-electrode system on a CHI760E electrochemical workstation (Chenhua). The working electrode was a RRDE (disk area: $0.2475\,cm^{-2}$ and Pt ring area: $0.1866\,cm^{-2}$), the counter electrode was graphite rod, with Hg/HgO and Ag/AgCl electrodes as reference electrode in alkaline and neutral electrolytes, respectively. The reference electrode was calibrated using a standard hydrogen electrode. Catalyst (2.0 mg) was dispersed into 1 mL of a mixed solution (isopropanol: water: 5 wt.% Nafion in a volume ratio of 8: 2: 1), then the resulting dispersions sonicated (400 W, 2 h) to obtain a uniform catalyst ink. Next, 10 μL ink was deposited onto the disk area of a RRDE electrode and the resulting modified electrode allowed to dried at room temperature (25 °C ± 3).

LSV curves were measured at 10 mV s^{-1}, 1600 rpm, with a potential of 1.2 V vs. RHE at the Pt ring, without resistance (R_s) compensation in O_2-saturated 0.1 M KOH or 0.1 M Na_2SO_4. The H_2O_2 selectivity and electron transfer numbers were calculated from LSV curves using the equations below.

$$H_2O_2 \, selectivity \, (\%) = 200 \times \frac{I_R/N}{I_D + I_R/N} \tag{1}$$

$$n = \frac{4|I_D|}{I_D + I_{R/N}} \tag{2}$$

where I_R, I_D and N representing the ring current, disk current, and collection efficiency (0.37), respectively.

H_2O_2 production tests at high current densities in a flow cell

A flow cell with anode/cathode compartments and a separator (Nafion 117 proton exchange membranes) was assembled and measured by one electrochemical station (BioLogic VMP3B). The membranes have the size of 1.5×3 cm with a thickness of 0.183 cm. The membranes were treated in 5 wt.% H_2O_2 at 80 °C for 1 hour and then soaked in DI water for 0.5 hour. The R_s of the flow cell was measured by iR compensation function in electrochemical workstation. The B_n-C catalyst ink (4 mg mL^{-1}) was sprayed on a working electrode (gas diffusion layer, HESEN HCP120, working area of 1 cm^2, and the concentration of 0.2 mg cm^{-2}). Ni foil electrode acted as anode electrode and Ag/AgCl electrode as reference electrode. 300 mL electrolyte (1.0 M KOH or 1.0 M Na_2SO_4) was added into anode/cathode compartments with a recycling rate of 20 mL min^{-1} by one pump. Pure O_2 was fed into the cathode compartment with a rate of 20 mL min^{-1}. The potentials were holden on 0.42 V and 0.1 V vs. RHE in alkaline and neutral electrolyte during the long-term stability measurement.

The H_2O_2 FE% was calculated according to the following equation:

$$FE\% = 2CVF/Q * 100\% \tag{3}$$

C, V, F, Q representing H_2O_2 concentration (mol L^{-1}), electrolyte volume (L), Faraday constant (96485 C mol^{-1}), total charge amount (C), respectively.

The H_2O_2 concentration was measured through a titration method according to the following reaction:

$$2Ce^{4+} + H_2O_2 \rightarrow 2Ce^{3+} + 2H^+ + O_2 \tag{4}$$
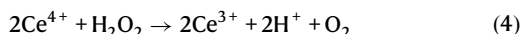
According to this reaction, the C_{H2O2} can be obtained based on the following equation:

$$C_{H2O2} = 1/2 \, \Delta C_{Ce4+} \tag{5}$$

The Ce^{4+} concentration was determined by one UV-vis spectrophotometer based on the absorbance at 317 nm.

Computational details

The DFT calculations were performed using Vienna ab initio simulation package (VASP)[52]. The electronic exchange-correlation potential was calculated using the Perdew-Burke-Ernzerhof (PBE) functional of generalized gradient approximation (GGA) were used[53–55]. The kinetic energy cutoff was set to 500 eV for the plane-wave basis set. The K-point sampling was obtained from the Monkhorst−Pack scheme with a ($3 \times 3 \times 1$) mesh for optimization. The tolerance of the self-consistent field (SCF) convergence was $1.0 \times e^{-5}$ eV, and the max force, stress and displacement were 0.02 eV Å^{-1}, 0.05 GPa and 0.001 Å, respectively. The supercell ($12 \text{ Å} \times 20 \text{ Å}$) of this system was composed of 5×8 unit cells

of graphene ($2.46 \text{ Å} \times 2.46 \text{ Å}$) and 4×5 unit cells of borophene ($2.50 \text{ Å} \times 4.00 \text{ Å}$). The vacuum layer was set around 20 Å to avoid the interaction along z-direction. After relaxation, the distance between graphene and borophene monolayer was ~2.0 Å, which implies weak van der Waals interaction between each layer.

The potential-dependence of reaction free energies in the elementary steps involving proton-electron transfers were evaluated using the computational hydrogen electrode (CHE) approach[56].

The Gibbs free energy was calculated using:

$$\Delta G = \Delta E_n + \Delta ZPE - T\Delta S \tag{6}$$

where ΔG is Gibbs free energy, ΔE_n is energy calculate from DFT, S is entropy, T is temperature (298.15 K), and ZPE is zero-point energy.

Black liquor depolymerization with H_2O_2 alkaline electrolyte

A flow cell was assembled and the FE% calculated according to the procedure described in the high production rate measurement with flow cell section above. The electrocatalytic synthesis of H_2O_2 was initiated by adding 300 mL of a 0.5 M KOH solution to both the anode and cathode chambers in a three-electrode flow cell. After the electrocatalytic operation of the cell for 1 hour, the reaction was stopped, and the FE% to H_2O_2 then was evaluated. Next, 43.5 mg of paper black liquor solid powder was added to the cathode chamber (concentration: 145 mg L^{-1}) and the electrocatalytic reaction was continued. As the electrolysis reaction proceeds, the yellow cathode solution gradually became colorless. When the solution became colorless, more black liquor powder was add to the cathode electrolyte (43.5 mg, 99.0 mg, and 87.0 mg of black liquor powder were added at the 5th, 11th, and 19th hours of the electrolysis reaction, with corresponding concentrations of 370 mg L^{-1}, 700 mg L^{-1}, 990 mg L^{-1}, respectively). The FE% of H_2O_2 production was measured in the 5 min time period prior to the addition of the black liquor powder. The entire electrolysis and black liquor powder degradation process were carried out in a water bath at 80 °C, with a total of four powder degradation cycles performed.

Data availability

All key data supports the figures within our paper and another finding in our study are included in the article and its Supplementary Information. Source data are provided as a Source Data file. Source data are provided with this paper.

References

1. Bu, Y. et al. Carbon-based electrocatalysts for efficient hydrogen peroxide production. *Adv. Mater.* **33**, e2103266 (2021).
2. Wen, Y. et al. Electrochemical reactors for continuous decentralized H_2O_2 production. *Angew. Chem. Int. Ed.* **61**, e202205972 (2022).
3. Li, L. et al. Tailoring selectivity of electrochemical hydrogen peroxide generation by tunable pyrrolic-nitrogen-carbon. *Adv. Energy Mater.* **10**, 2000789 (2020).
4. Chen, S. et al. Defective carbon-based materials for the electrochemical synthesis of hydrogen peroxide. *ACS Sustainable Chem. Eng.* **6**, 311–317 (2018).
5. Wu, J. et al. A metal-free electrocatalyst for carbon dioxide reduction to multi-carbon hydrocarbons and oxygenates. *Nat. commun.* **7**, 13869 (2016).
6. Zhao, Y. et al. Carbon catalysts empowering sustainable chemical synthesis via electrochemical CO_2 conversion and two-electron oxygen reduction reaction. *Small*, 2311163 https://doi.org/10.1002/smll.202311163 (2024).
7. Iglesias, D. et al. N-doped graphitized carbon nanohorns as a forefront electrocatalyst in highly selective O_2 reduction to H_2O_2. *Chem* **4**, 106–123 (2018).

8. Wu, Q. et al. Unveiling the dynamic active site of defective carbon-based electrocatalysts for hydrogen peroxide production. *Nat. commun.* **14**, 6275 (2023).

9. Chen, S. et al. Chemical identification of catalytically active sites on oxygen-doped carbon nanosheet to decipher the high activity for electro-synthesis hydrogen peroxide. *Angew. Chem. Int. Ed.* **60**, 16607–16614 (2021).

10. Guo, Y. et al. Ultrahigh oxygen-doped carbon quantum dots for highly efficient H_2O_2 production via two-electron electrochemical oxygen reduction. *Energ. Environ. Sci.* **15**, 4167–4174 (2022).

11. Xia, Y. et al. Highly active and selective oxygen reduction to H_2O_2 on boron-doped carbon for high production rates. *Nat. commun.* **12**, 4225 (2021).

12. Yu, X. et al. Boron-doped graphene for electrocatalytic N_2 reduction. *Joule* **2**, 1610–1622 (2018).

13. Lu, S. et al. Unveiling the structural transformation and activity origin of heteroatom-doped carbons for hydrogen evolution. *PNAS* **120**, e2300549120 (2023).

14. Wu, T. et al. Anisotropic boron–carbon hetero-nanosheets for ultrahigh energy density supercapacitors. *Angew. Chem. Int. Ed.* **59**, 23800–23809 (2020).

15. Fan, Q. et al. High-yield production of few-layer boron nanosheets for efficient electrocatalytic N_2 reduction. *Chem. Commun.* **55**, 4246–4249 (2019).

16. Wu, R. et al. Micrometre-scale single-crystalline borophene on a square-lattice Cu(100) surface. *Nat. Chem.* **14**, 377–383 (2022).

17. Zhang, X. et al. Boron nanosheet: An elemental two-dimensional (2D) material for ambient electrocatalytic N_2-to-NH_3 fixation in neutral media. *ACS Catal.* **9**, 4609–4615 (2019).

18. Joshi, A. et al. Engineering oxygen defects in the boron nanosheet for stabilizing complex bonding structure: An approach for high-performance supercapacitor. *Chem. Eng. J.* **407**, 127122 (2021).

19. Chahal, S. et al. Borophene via micromechanical exfoliation. *Adv. Mater.* **33**, 2102039 (2021).

20. Fan, M. et al. A facile "Double Catalysts" approach to directionally fabricate pyridinic N-B pair doped crystal graphene nanoribbons/amorphous carbon hybrid electrocatalysts for efficient oxygen reduction reaction. *Adv. Mater.* **34**, e2107040 (2022).

21. Wu, Y. et al. Boron–sulfur pairs for highly active 2e⁻ oxygen reduction reaction to electrochemically synthesize hydrogen peroxide. *ACS Sustainable Chem. Eng.* **11**, 13363–13373 (2023).

22. Li, X. et al. Synthesis of graphene films on copper foils by chemical vapor deposition. *Adv. Mater.* **28**, 6247–6252 (2016).

23. Liang, C. et al. Mesoporous carbon materials: Synthesis and modification. *Angew. Chem. Int. Ed.* **47**, 3696–3717 (2008).

24. Kamiyama, A. et al. MgO-template synthesis of extremely high capacity hard carbon for Na-Ion battery. *Angew. Chem. Int. Ed.* **60**, 5114–5120 (2021).

25. Ji, X. et al. A novel top-down synthesis of ultrathin 2D boron nanosheets for multimodal imaging-guided cancer therapy. *Adv. Mater.* **30**, 1803031 (2018).

26. Wu, Y. A. et al. Large single crystals of graphene on melted copper using chemical vapor deposition. *ACS Nano* **6**, 5010–5017 (2012).

27. Tao, Y. et al. A solvent decomposition and explosion approach for boron nanoplate synthesis. *Chem. Commun.* **57**, 4922–4925 (2021).

28. Feng, B. et al. Experimental realization of two-dimensional boron sheets. *Nat. Chem.* **8**, 563–568 (2016).

29. Hou, C. et al. Ultrastable crystalline semiconducting hydrogenated borophene. *Angew. Chem. Int. Ed.* **59**, 10819–10825 (2020).

30. Mu, Y. & Li, S.-D. First-principles study on the oxidation of supported β_{12}-borophene. *J. Phys. Chem. C* **124**, 28145–28151 (2020).

31. Li, L. et al. Chemically identifying single adatoms with single-bond sensitivity during oxidation reactions of borophene. *Nat. commun.* **13**, 1796 (2022).

32. Han, C. et al. 2D boron nanosheet architectonics: Opening new territories by smart functionalization. *J. Mater. Chem. A* **10**, 2736–2750 (2022).

33. Liu, M. et al. Boron K-edge XANES of boron oxides: Tetrahedral B–O distances and near-surface alteration. *Phys. Chem. Miner.* **28**, 421–427 (2001).

34. Ray, S. C. et al. X-Ray absorption studies of boron–carbon–nitrogen ($B_xC_yN_z$) ternary alloys. *Diam. Relat. Mater.* **13**, 1553–1557 (2004).

35. Lan, J. et al. Nanoporous $B_{13}C_2$ towards highly efficient electro-chemical nitrogen fixation. *Small* **17**, 2102814 (2021).

36. Zhang, B. et al. Graphene-layer-coated boron carbide nanosheets with efficient electromagnetic wave absorption. *Appl. Surf. Sci.* **560**, 150027 (2021).

37. Dai, Y. et al. Manipulating local coordination of copper single atom catalyst enables efficient CO_2-to-CH_4 conversion. *Nat. commun.* **14**, 3382 (2023).

38. Cheng, L. et al. Steering the topological defects in amorphous laser-induced graphene for direct nitrate-to-ammonia electro-reduction. *ACS Catal.* **12**, 11639–11650 (2022).

39. Huang, L. et al. Direct synthesis of ammonia from nitrate on amorphous graphene with near 100% efficiency. *Adv. Mater.* **35**, 2211856 (2023).

40. Sa, Y. J., Kim, J. H. & Joo, S. H. Active edge-site-rich carbon nanocatalysts with enhanced electron transfer for efficient electrochemical hydrogen peroxide production. *Angew. Chem. Int. Ed.* **58**, 1100–1105 (2019).

41. Lu, Z. et al. High-efficiency oxygen reduction to hydrogen peroxide catalysed by oxidized carbon materials. *Nat. Catal.* **1**, 156–162 (2018).

42. Xia, C., Kim, J. Y. & Wang, H. Recommended practice to report selectivity in electrochemical synthesis of H_2O_2. *Nat. Catal.* **3**, 605–607 (2020).

43. Li, Z. et al. Resource value flow analysis of paper-making enterprises: A Chinese case study. *J. Clean. Prod.* **213**, 577–587 (2019).

44. Ma, Q. et al. Recycling of waste bamboo biomass and papermaking waste liquid to synthesize sodium lignosulfonate/chitosan glue-free biocomposite. *Molecules* **28**, 6058 (2023).

45. Deepa, A. K. & Dhepe, P. L. Lignin depolymerization into aromatic monomers over solid acid catalysts. *ACS Catal.* **5**, 365–379 (2014).

46. Zhang, C. & Wang, F. Catalytic lignin depolymerization to aromatic chemicals. *Acc. Chem. Res.* **53**, 470–484 (2020).

47. Guan, M.-H. et al. Boosting selective oxidation of ethylene to ethylene glycol assisted by in situ generated H_2O_2 from O_2 electro-reduction. *Angew. Chem. Int. Ed.* **62**, e202302466 (2023).

48. Fan, M. et al. N-B-OH site-activated graphene quantum dots for boosting electrochemical hydrogen peroxide production. *Adv. Mater.* **35**, 2209086 (2023).

49. Jing, L. et al. Dual-engineering of porous structure and carbon edge enables highly selective H_2O_2 electrosynthesis. *Adv. Funct. Mater.* **33**, 2305795 (2023).

50. Dong, K. et al. Honeycomb carbon nanofibers: A superhydrophilic O_2-entrapping electrocatalyst enables ultrahigh mass activity for the two-electron oxygen reduction reaction. *Angew. Chem. Int. Ed.* **60**, 10583–10587 (2021).

51. Song, D. et al. Carboxylated carbon quantum dot-induced binary metal–organic framework nanosheet synthesis to boost the electrocatalytic performance. *Mater. Today* **54**, 42–51 (2022).

52. Kresse, G. & Joubert, D. From ultrasoft pseudopotentials to the projector augmented-wave method. *Phys. Rev. B* **59**, 1758–1775 (1999).

53. Kresse, G. & Furthmüller, J. Efficient iterative schemes for ab initio total-energy calculations using a plane-wave basis set. *Phy. Rev. B* **54**, 11169–11186 (1996).

54. Sprik, M. & Ciccotti, G. Free energy from constrained molecular dynamics. *J. Chem. Phys.* **109**, 7737–7744 (1998).

55. Hammer, B., Hansen, L. B. & Nørskov, J. K. Improved adsorption energetics within density-functional theory using revised Perdew-Burke-Ernzerhof functionals. *Phys. Rev. B* **59**, 7413–7421 (1999).

56. Nørskov, J. K. et al. Origin of the overpotential for oxygen reduction at a fuel-cell cathode. *J. Phys. Chem. B* **108**, 17886–17892 (2004).

Author contributions

M.F. conceived the idea. Y.W. performed the preparation of catalysts. Y.W., Q.Y. and S.H. performed the electrochemical measurements including RRDE and flow cell. Z.W. and Y.Z. completed the DFT simulation. A.W. and K.S. helped the electrochemical analysis. G.W., J.W. helped to polish the draft. J.W. and J.J. helped to design experiments. M.F. wrote the manuscript with input from all co-authors.

Competing interests

The authors declare no competing interests

Additional information

Supplementary information The online version contains supplementary material available at https://doi.org/10.1038/s41467-024-55071-7.

Correspondence and requests for materials should be addressed to Ziyun Wang, Jingjie Wu, Jianchun Jiang or Mengmeng Fan.

Peer review information *Nature Communications* thanks Hao Li, and the other, anonymous, reviewers for their contribution to the peer review of this work. A peer review file is available.

Reprints and permissions information is available at http://www.nature.com/reprints

Publisher's note Springer Nature remains neutral with regard to jurisdictional claims in published maps and institutional affiliations.